A three component-based van der Waals surface vertically designed for biomolecular recognition enhancement

Ayaz Hassan[†], Lucyano J. A. Macedo[†], Isabela A. Mattioli[†], Rafael J. G. Rubira[#], Carlos J. L. Constantino[#], Rodrigo G. Amorim[§], Filipe C. D. A. Lima[‡], Frank N. Crespilho[†]*

[†]São Carlos Institute of Chemistry, University of São Paulo, 13560-970 São Paulo, Brazil

[§]Physics Departament, ICEx, Fluminense Federal University – UFF, Volta Redonda, 27213-145, Rio de Janeiro, Brazil

[‡]Federal Institute of Education, Science, and Technology of São Paulo, Campus Matão, 15991-502 São Paulo, Brazil

[#]Physics Department, São Paulo State University-UNESP, Campus of Presidente Prudente, SP 19060-900, Brazil

ABSTRACT

Graphene-based vertical electrodes may have applications in biomolecular recognition for producing low-cost biodevices with high electronic conductivity. However, they are unsuitable for measuring small interfacial capacitance variations because graphene is mostly composed of basal sp^2 carbon surface, which limits its sensitivity as an electrochemical biosensor. Herein, we introduce an unconventional device alternative based on a three-component vertically designed (TCVD) surface comprising ferrocene/graphene/gold deposited on SiO_2/Si wafers. Ferrocene is the top layer that promotes reversible redox communication with the electrolyte, while graphene–gold is the strategically projected layer underneath. Bader charge analysis indicated that graphene donates electronic density to the gold surface, thereby significantly increases the charge transfer exchange rate with ferrocene. The TCVD surface is much more reactive and sensitive to charge variations compared with pristine graphene, and it maintains excellent conductive properties. The TCVD device was used to detect DNA hybridization in solutions, since this is well-known to be a challenging process on a pristine graphene vertical device. A TCVD device can detect small interfacial charge perturbations from DNA hybridization. Based on quantum mechanics calculations combined with spectromicroscopy data, it was realized that the unique synergic interaction between gold and graphene amplified biomolecular recognition, whereby DNA in nanomolar range concentration correlated to 0.8 ± 0.1 μF cm^{-2}, which was effortlessly detected. This result is promising since 3.0 μF cm^{-2} is the limit of quantum capacitance for bare graphene. Notably, these results open a new possibility for next-generation TCVD bioelectronics based on van der Waals surfaces, while further innovation and material scrutiny may lead to the achievement of TCVD devices with robust biomolecular recognition abilities.

Keywords: van der Waals surface, graphene, capacitance, ferrocene, DNA biosensor

INTRODUCTION

Electrolyte-gated graphene field-effect transistors (GFETs) [1] have been widely described in the last decade for the electrical detection of chemical and biological species. The main advantage of GFETs is that molecular interaction between the analyte and basal-plane graphene surface is detectable through the employment of small conductance changes[2]. However, the manufacture of practical label-free biosensors requires a very expensive approach for devices, with complex architectures[3], clean room infrastructure[4], and nanolithography procedures[5]. On the other hand, conventional graphene-based vertical electrodes that do not adopt the field-effect approach are very attractive for label-free biomolecular recognition applications. These devices are very simple and inexpensive to fabricate, with possibilities to produce devices with large areas[6], while avoiding complex micro- and nanolithography procedures[7]. The limitation of graphene-based vertical devices ensues from the low charge transfer ability of graphene to migrate electrons outside the plane[8], perpendicularly to the basal-plane. This is because, contrary to the GFET, vertical electrodes use the graphene layer as a charge collector or electrified interface (electrode/electrolyte) and perturbations from the molecular interaction with an analyte.

The layer-by-layer stacking of van der Waals (vdW) surfaces with graphene has recently introduced some new prospects toward the construction of vertical devices[9]. Various tunneling devices, such as GFET, gate-controlled triode, and spin-valve mechanisms, based either on simple bilayer graphene or with an insulating barrier in the middle, and vertically aligned graphene on Si heterostructures have been investigated to achieve high on/off switching ratios in the resultant devices[10–12]. From a theoretical perspective, the adsorption of graphene on metal surfaces, particularly Au, occurs weakly and is mainly considered as physisorption with an equilibrium separation distance of 0.331 nm and binding energy of 30 meV[13], thereby preserving the electronic structure of graphene, in addition to retaining the high conductivity of the metallic substrate. Weak vdW interactions between the bottom layer Au and top layer graphene do not disturb the charge carrier mobility of the latter, and in some cases, improve the charge carrier transfer at theinterface between the two layers, which can then be harnessed in efficient sensor and biosensor applications.

Motivated by the above-mentioned considerations, herein, we report the development of a new type of vertical device with unique physical-chemical properties, i.e., the three-component vertically designed (TCVD) device, whose surface comprises ferrocene/graphene/gold components deposited on SiO_2/Si wafers. Ferrocene is the top layer that promotes reversible redox communications between the electrolyte and the graphene layer. Our TCVD device is sensitive to small surface charge variations that are

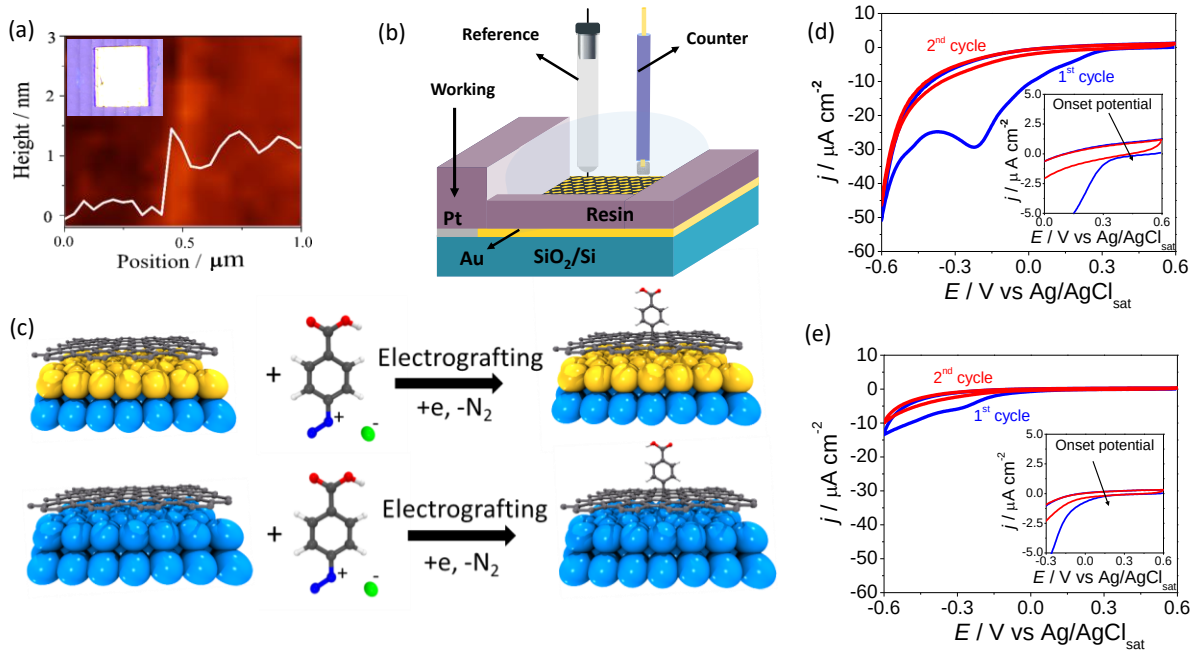

Figure 1. TCVD device fabrication and reactivity test. (a) Example of one height profile in the boundary region between SiO_2/Si and graphene. Inset: Optical microscopic image of Gr/Au/SiO_2/Si (b) Schematic of the experimental setup used during the electrochemical characterization composed of graphene supported on SiO_2/Si-modified Au (Gr/Au/SiO_2/Si) as the working electrode, Ag/$AgCl_{sat}$ as the reference electrode, and Pt wire as the counter electrode; (c) Reaction mechanism for the electrochemical grafting of 4-carboxyphenyl radicals to the graphene sheets in Gr/Au/SiO_2/Si (top) and Gr/SiO_2/Si (bottom) electrodes; Cyclic voltammograms obtained during the covalent functionalization of the electrodes: (d) Gr/Au/SiO_2/Si and (e) Gr/SiO_2/Si, performed electrochemically in the reaction mixture containing 4-amino benzoic acid, $NaNO_2$, and H_2SO_4 in the potential range of +0.6 – -0.6 at a scan rate of 50 mV s^{-1} during two cycles.

undetectable by the individual pristine components. The origin of the interactions among the component layers is investigated via spectroscopy, microscopy, electrochemistry, and density-functional theory (DFT) simulation. The biosensing property of the device is investigated through the measurements of variation in the interfacial capacitance induced by the adsorption of biological molecules at the extremely sensitive vdW surface.

RESULTS

Enhanced chemical reactivity of the graphene on Au. Large area (~10 mm^2) chemical vapor deposition (CVD)-grown monolayer graphene from a Cu substrate was transferred through a wet chemical procedure to the SiO_2/Si substrate lithographically modified with a metal (Au) subsurface. Comparatively, a monolayer graphene electrode was also prepared on SiO_2/Si. The obtained graphene sheets are uniform in both cases, with very few structural defects present (Fig. S1), presuming that Au is entirely covered by the

monolayer graphene sheet. Figure 1a shows the atomic force microscopic (AFM) image at the boundary region between SiO_2/Si and graphene, and the optical microscopic image of Gr/Au/SiO_2/Si (inset).

One effective way to verify if the Au underneath the graphene enhances electron transfer is to promote a controlled functionalization on the basal plane of graphene, using a three-electrode cell, as shown schematically in Figure 1b. Therefore, covalent electron transfer chemistry of graphene with diazonium salts was conducted[14]. Figure 1c shows the reaction mechanism for the reduction of 4-carboxyphenyl diazonium chloride, wherein the 4-carboxyphenyl radicals are attached to the electrode surface. The values of onset potential, reduction peak current density, and surface coverage values calculated from the cyclic voltammograms (CVs) for both electrodes (Fig. 1d-e) are shown in Table S1. The enhanced chemical reactivity of the graphene on the Au electrode is initially observed from the values of onset potential, where this electrode depicts a more positive onset value (ca. 250 mV) as compared to the value of ca. 50 mV for the Gr/SiO_2/Si (Figs 1d-e, insets). The difference in the chemical reactivity of these two dissimilar electrodes during the covalent electron transfer is also observed from the magnitude of the current densities in their respective CVs, which exhibit a four times higher value of current density for the Gr/Au/SiO_2/Si compared to the conventional Gr/SiO_2/Si electrode. This is further confirmed by the more than 10 times higher value of surface concentration (4.3×10^{-9} mol cm^{-2}) calculated for the Gr/Au/SiO_2/Si relative to the value ca. 2.3×10^{-10} mol cm^{-2} obtained for the Gr/SiO_2/Si electrode. From the comparison of these results with those of the pure metallic Au surface without graphene (Table S1 and Fig. S2), it is inferred that a synergetic effect exists between the graphene and underneath metallic substrate, thereby improving overall chemical reactivity. These results are corroborated by micro-Raman (Fig. 2a) and micro-Fourier-transform infrared (FTIR) (Fig. 2b) spectroscopies, as evidenced by the attachment of many functional groups to its surface.

Micro-Raman spectra were recorded for the pristine and functionalized electrodes to confirm the monolayer graphene, based on the position of the 2D band[15], which appears in the region between 2,650–2,700 cm^{-1} for the single layer graphene. The interaction between the graphene and the underlying substrate is then determinable from the calculation of full-width at half maximum (FWHM) of the same 2D band. A weaker interaction with the underlying substrate could lead to a larger shift in the position of this band[16], a phenomenon that we observed for the graphene on Au electrode after it was chemically functionalized. The weaker interaction of the graphene with Au is also evident from the lower intensity of the various bands observed in the Raman spectra. However, for Gr/SiO_2/Si, the observed shift in the position of the bands, particularly the 2D band, is relatively small after functionalization occurs. These results paralleled the previously calculated theoretical data, where the weaker interaction between the metal (Au) substrate and

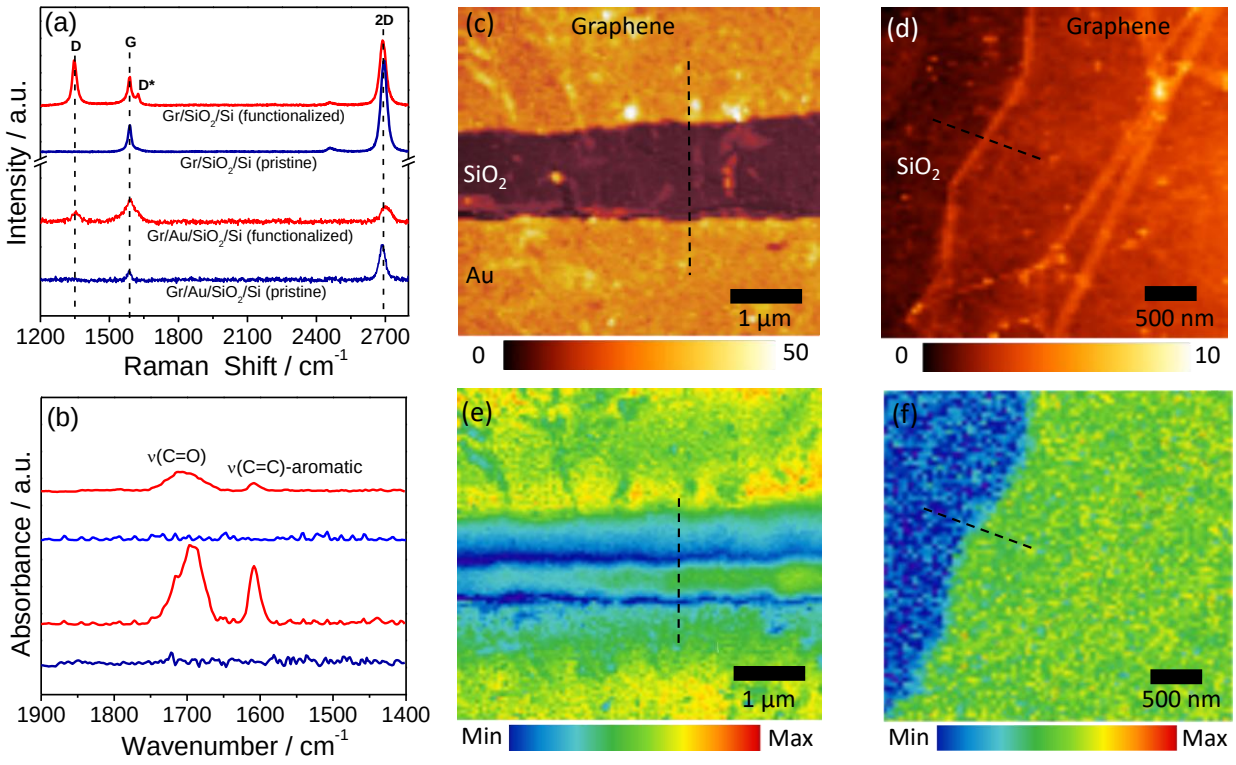

Figure 2. (a) Micro-Raman spectra and (b) micro-FTIR spectra of Gr/Au/SiO_2/Si (bottom) and Gr/SiO_2/Si (top) electrodes. (blue) Pristine graphene (red) 4-carboxyphenyl functionalized graphene; AFM and s-SNOM images of the graphene on lithographically decorated Au on SiO_2/Si and SiO_2/Si substrates (c) Topography and (e) IR broadband image in the boundary region between Au and SiO_2/Si (d) Topography (f) IR broadband image in the boundary region between SiO_2/Si and graphene.

graphene was attributed to the binding energy of 13 meV per carbon atom[17]. This value is approximately six times lower than the binding energy of graphene on SiO_2/Si[18].

The value of the I_D/I_G ratio calculated from the Raman spectrum can provide an estimate of the number of defects in the graphene, which is directly proportional to the density of the defects in the graphene sheets. By using this parameter, the defects in the graphene on Au and without Au can be quantified through the application of a mathematical approach (see SI, section S3). A larger defect density value (ca. 9.4×10^{-13} mol cm^{-2}) for the functionalized graphene on SiO_2/Si compared to the value of 2.5×10^{-13} mol cm^{-2} for the graphene on Au/SiO_2/Si, suggests an increased disorder in the former case after functionalization occurred. These results do not corroborate the values of the surface concentration of 4-carboxyphenyl species incorporated into graphene electrodes, calculated from their respective CV profiles (i.e., 4.3×10^{-9} and 2.3×10^{-10} mol cm^{-2} for the graphene on Au and without Au, respectively). It is noteworthy that although the Raman spectra are taken from several different regions of the graphene sheet, they do not represent the entire bulk surface of the electrode, particularly after functionalization. These results are in accordance with

the previous studies that present that covalent functionalization occurs inhomogeneously on the electrode surface[19]. Micro-FTIR spectra were recorded for the pristine electrodes, where no infrared (IR) peaks were observed (Fig. 2b, blue lines) due to the lack of IR active vibrational modes in the graphene structure. However, the covalently functionalized graphene electrodes show two vibrational modes at 1705 cm^{-1} and 1605 cm^{-1} in the IR spectra (Fig. 2b, red lines). These vibrational modes are indicative of the attachment of the 4-carboxyphenyl to the graphene sheets. This is because both observed peaks are located at the position, characteristics of C=O and C=C (aromatic) stretching modes, present in the structure of the organic functional group. As these analyses were performed at several different locations of the pristine and functionalized graphene sheets supported on Au (in Gr/Au/SiO_2/Si electrode), the results allow us to state, at this point, that the graphene sheet on Au is physically intact and continuous. However, the extent to which it interacts with the Au and its chemical reactivity are different from those of graphene on SiO_2/Si, with the interaction mainly being through weak forces.

Further insight into the interaction between the components, was obtained through scattering-type scanning near field optical microscopy (s-SNOM) experiments. For this, we selected an area entirely covered by the graphene sheet at the border region between SiO_2/Si and Au in the Gr/Au/SiO_2/Si (Fig. 2c), as well as between graphene and SiO_2/Si in the Gr/SiO_2/Si electrode (Fig. 2d). Initially, AFM images were recorded to measure the topography of these portions of the electrodes. An average height of approximately 2 nm observed for the graphene sheet on SiO_2/Si is relevant to the thickness of monolayer graphene sheet (Figs. 2d and S4c), which reaches approximately 5 nm and 10 nm on the basal plane and the edges, respectively, when the graphene is covalently functionalized (Figs. S4e and S4g). The average height of graphene on Au is approximately 32 nm, which is due to the 30 nm thickness of the Au film and 2 nm of the graphene sheet (Figs. 2c and S4a). Nanoscale IR optical images were recorded simultaneously by modulating the obtained optical signal via the oscillation of the AFM tip, followed by demodulating at the second harmonic of the tip frequency. The s-SNOM measurements are normalized by dividing the measured amplitude of the sample (graphene) with that of the reference (Au), i.e., $\sigma_G(\omega) = \sigma(\omega)/\sigma_{Au}(\omega)$. An increase in the optical intensity is achieved in the s-SNOM images, either if going from graphene on SiO_2/Si toward graphene on Au (Fig. 2e) or from bare SiO_2/Si toward the graphene on SiO_2/Si (Fig. 2f). The difference in the relative s-SNOM amplitude of graphene on different surfaces is attributed to the different degrees of polaritonic coupling of the graphene plasmons with the phonons of the underlying surface. On the one hand, the contrast in the optical signal can be easily observed between graphene on SiO_2/Si (Figs. 2f and S4d). On the other hand, the higher intensity of the optical signal for the graphene on Au than on SiO_2/Si is due to the greater scattering properties of the former. Unexpectedly, the optical intensity is drastically decreased

at the border regions between the Au and SiO_2/Si (Figs. 2e and S4b), which may be due to the weaker coupling between the graphene and the substrate at these regions, wherein graphene mostly exists in a suspended form.

Influence of Au subsurface on the electrochemical properties. Solution electrochemistry using $[Fe(CN)_6]^{3-/4-}$ was performed to investigate the charge transfer mechanism on bare graphene and graphene with Au underneath. As expected for the monolayer graphene, the absence of a redox couple (Fig. 3a, blue line) indicates the poor HET properties of this material. The low electrochemical activity of pristine graphene is due to the presence of low density of states (DOS)/defects or oxygenated functional groups, which are mostly considered to be detrimental for the efficient electron transfer process. As depicted by the micro-Raman spectrum, the surface concentration of the edge defects in the obtained graphene sheet is very low, which consequently contributes minimally to the electron transfer process of the $[Fe(CN)_6]^{3-/4-}$ redox probe, commonly considered as a surface-sensitive[20] redox probe. Such an electrochemical behavior is also likely to be observed on the basal plane of highly oriented pyrolytic graphite. These carbonaceous materials exhibit similar structures with low global coverage of defect sites, and hence, their steady state voltammetric responses have been observed, while using the redox routes[21–23].

Contrary to the graphene on the SiO_2/Si electrode, a peak-shaped CV was observed for the graphene on Au with a well-defined redox couple (Fig. 3a, red line) exhibiting a peak-to-peak separation, ΔE_p value of ca. 411 mV. The ΔE_p value, a qualitative measure of the electrochemical activity, reveals a much faster electron transfer process of the graphene, attributed to the increase in its electronic DOS, provided by the presence of Au. This change in the electronic DOS shifts the position of the graphene Fermi level, which occurs more probably through the charge-doping of the Au with graphene[24]. This is because of the difference in their work functions, which changes the electrochemical potential of the graphene electrons,[25] and hence, improves its electron transfer properties to the redox probe. Several theoretical investigations have shown that the interaction between the graphene and the metal occurs either through physisorption, with no change in the graphene band structure or through chemisorption, where a new surface phase is formed[13,24]. For graphene and Au, the physisorption model fits the best, as it does not significantly interrupt the band structure of the graphene, and hence, the Fermi level is only shifted slightly[26]. Comparative electrochemical impedance spectroscopy (EIS) analysis of the graphene electrodes was performed by using the $[Fe(CN)_6]^{3-/4-}$ redox species in solution. From the Nyquist plot (Fig. 3b, blue curve), which exhibits only a linear profile, it can be inferred that pristine monolayer graphene lacks vertical electron transfer properties. However, for the graphene on Au electrode (Fig. 3b, red curve), a semicircle in the higher

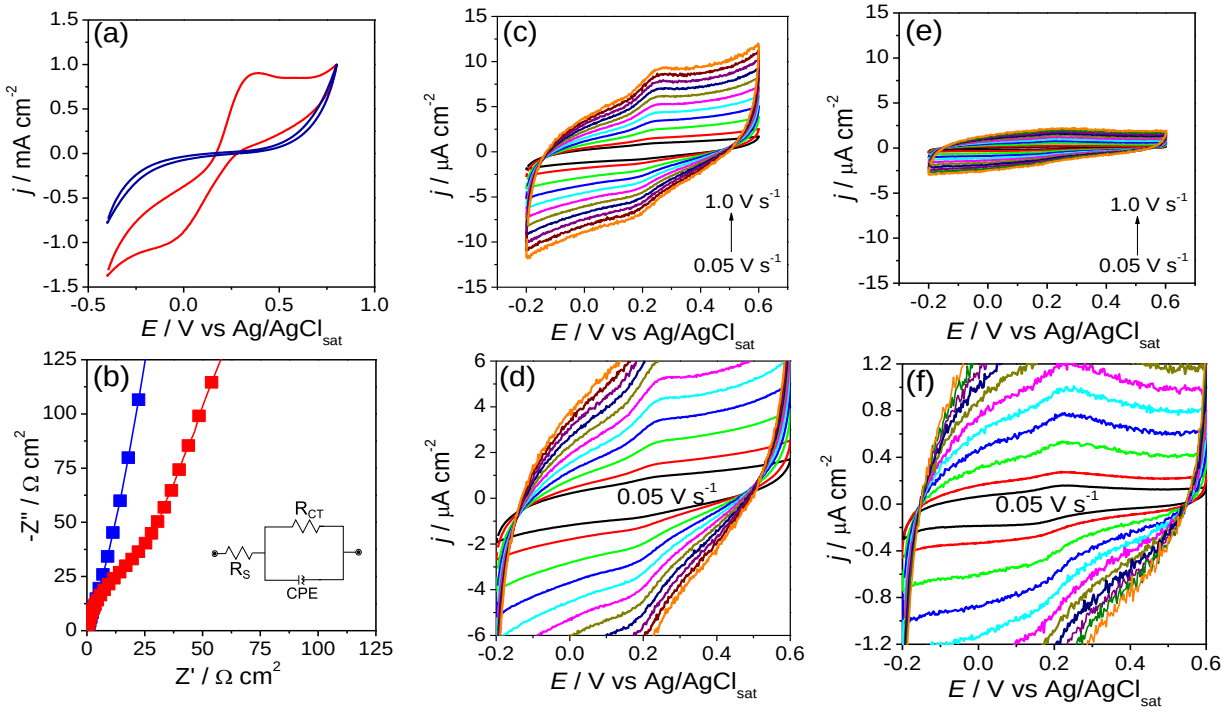

Figure 3. (a) Cyclic voltammograms and (b) EIS spectra of the electrodes Gr/SiO_2/Si (blue) and Gr/Au/SiO_2/Si (red) in $[Fe(CN)_6]^{4-/3-}$ (1×10^{-3} mol.L^{-1}) and KCl (1×10^{-1} mol.L^{-1}). Scan rate: 100 mV s^{-1}; Cyclic voltammograms of (c-d) Gr/Au/SiO_2/Si and (e-f) Gr/SiO_2/Si with ferrocene (25 mmol.L^{-1}) on the surface of the electrodes in KCl (0.1 mol.L^{-1}) in the potential range of -0.2 – +0.6 V at different potential scan rates.

frequency region appears. The development of the semicircle indicates the electron transfer process to occur between the electrode surface and redox probe. These results are consistent with the CV experiments previously obtained for this electrode. The value of charge transfer resistance (R_{CT}) of 8.83 Ω cm^2 was calculated from the EIS spectrum by the simulation of the equivalent circuits for the Gr/Au/SiO_2/Si electrode (inset of Fig. 3b). This value is comparable to the R_{CT} value of 13.07 Ω obtained for the monolayer graphene supported on a Au modified glass substrate[27]. Further electrochemical experiments were performed to determine the possibility of the Au in the Gr/Au/SiO_2/Si electrode to directly contact the electrolyte solution through holes and tears within the covered region and display the impact of the exposed Au on the electrochemical process. Thus, an electrode having a Au subsurface underneath and partially covered by the graphene sheet was prepared (Fig. S5). From the CV recorded in $[Fe(CN)_6]^{4-/3-}$, a ΔE_p value of 270 mV was obtained (Fig. S6a, blue line). Comparing the ΔE_p values obtained for graphene on Au with and without an exposed Au area, a greater reversibility was observed in the former case. This indicates a faster HET when the Au surface is in direct contact with the electrolyte solution compared with the Au surface that was completely covered by the graphene sheet. The Gr/Au/SiO_2/Si electrode behaves

electrochemically different from the bare thin Au film electrode based on CV, and the corresponding ΔE_p values decreased from ca. 411 mV for the graphene on Au to 115 mV for the Au electrode (Fig. S6a, red line). The corresponding EIS spectra for the graphene on Au with the exposed Au area and the thin Au film electrode (Fig. S6b) display a difference in the Nyquist plots from that of Gr/Au/SiO_2/Si electrode. The appearance of well-defined semicircles indicates a decrease in the R_{CT}, and hence, a change in the electrochemical behavior of the two electrodes. Thus, by comparing the ΔE_p values of all these electrodes, it can be inferred that the electrochemical activity of the redox probe at the electrode surface follows a descending order: Au film electrode > Gr/Au/SiO_2/Si with exposed Au area > Gr/Au/SiO_2/Si > Gr/SiO_2/Si.

TCVD device: Ferrocene layer and electron transfer mechanism. Efficient charge transfer occurs from the underlying substrate (Au) to the graphene, and then, to the solution, as observed from electrochemical experiments using the $[Fe(CN)_6]^{3-/4-}$ redox probe. To create an electrochemically active surface, we use ferrocene molecules because they can adsorb on graphene sheets through non-covalent π-π interactions. With a ferrocene/gold/graphene configuration, we obtain a typical TCVD device, the fabrication of which is quite simple and does not require a clean room or nanolithography technique. Summarily, the experimental procedure is based on a direct drop-casting procedure involving the deposition (μL) of the ferrocene onto the graphene surface. Thereafter, the quality test for TCVD is based on merely recoding the CV.

CVs obtained for the TCVD are shown in the Figures 3c-d and compared with the conventional graphene on the SiO_2/Si electrode (Figs. 3e-f). In both cases, oxidation and reduction peaks are observed, which are assigned to the ferrocene molecules adsorbed on the graphene surface. Initially, a typical decrease in the current density was observed by cycling the electrodes up to 200 cycles (Figs. S7a-b show the last 50 cycles), thereby indicating the desorption of weakly adsorbed molecules from the surface of the electrodes. Interestingly, the rate of dissolution of ferrocene from the surface of TCVD is much slower than that of the Gr/SiO_2/Si electrode, as observed from the larger decrease in the current density of the CV profile in the latter case. This confirms that ferrocene has a much stronger affinity toward the graphene on the Au surface. Here, it is reasonable to submit that the vdW forces play a crucial role in the adsorption of graphene on Au, in addition to the interaction between the graphene and ferrocene in the case of TCVD. In the latter cases, the interactions most probably occur between the carbon rings present in the structure of graphene and ferrocene. In all these scenarios, the underlying Au plays a major role in the adsorption process. The vdW surface develops; thus, it can provide a suitable platform for the efficient adsorption of biomolecules to the graphene surface, which is sufficiently stable in the case of TCVDs compared to that of graphene on

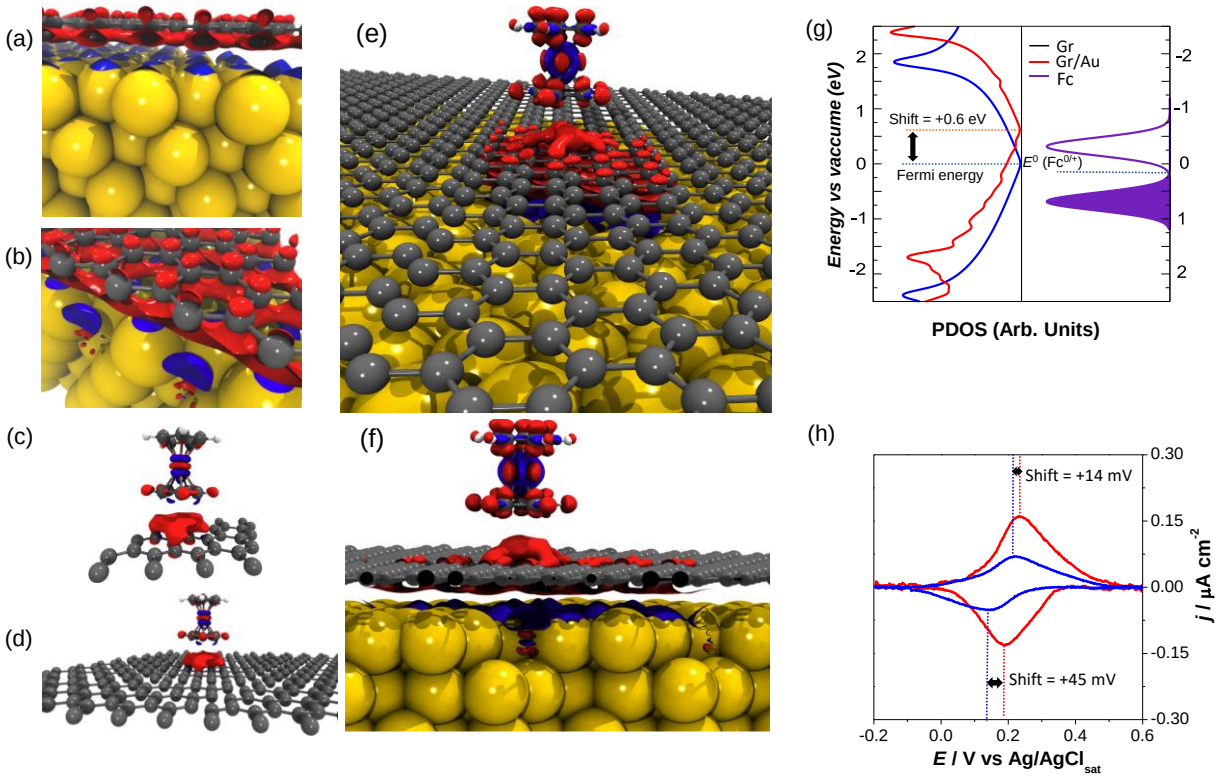

Figure 4: Charge density difference for the systems: a-b) graphene monolayer and Au (111); c-d) Ferrocene and monolayer graphene; e-f) Ferrocene, monolayer graphene and Au (111). Atomic color representation: Au (yellow), C (gray), H (white), and Fe (orange). Blue and red spheroids indicate charge difference accumulation and depletion, respectively. For easy visualization, the whole system was expanded periodically, and the ferrocene and the charge density were kept for only one supercell; (g) Simulated density of states of monolayer graphene (blue) and monolayer graphene on Au (red), as well as the density distribution of the occupied (reduced) and unoccupied (oxidized) states of ferrocene (grey). The simulation parameters used for calculating the DOS of ferrocene were: E0 ($Fc^{0/+1}$) = 0.185 V vs $Ag/AgCl_{sat}$, λ = 0.5 and T = 298 K. (h) Cyclic voltammograms of ferrocene after the subtraction of background current for the Gr (blue) and Gr on Au (red).

a SiO_2/Si surface. The difference in the HET kinetics of the top layer ferrocene on the graphene surface in both cases was evaluated by applying a mathematical approach introduced by Laviron (SI, S8). The values of k^0 obtained are 3.8 s^{-1} and 1.4 s^{-1} for TCVD and Gr/SiO_2/Si, respectively, indicating faster electron transfer kinetics for the adsorbed ferrocene on the surface of graphene in the first case, whereby the Au is present underneath compared to the electrode, which simply denotes the graphene on SiO_2/Si.

To provide further insights into the possible charge transfer mechanism on the Au, graphene, and the Fc of the TCVD device, theoretical models in the Kohn-Sham scheme of the DFT were employed. These results are shown on the qualitative and quantitative levels. From a qualitative perspective, the charge density differences are shown in the Figure 4. The Gr-Au model (Fig. 4a-b) indicates that the charge transfer is delocalized through the entire surface, thereby maintaining the symmetry and electronic distribution of

the Gr and generating an attractive behavior. For the Fc@Gr system (Fig. 4c-d), the charge density is localized between the Fc and the graphene, it also presents attractive characteristics. Analyzing the entire system, Fc@Gr-Au (Fig. 4e-f), there is a charge localization over the Fc molecule, which is placed on top of the graphene monolayer. Comparing the models, Fc@Gr and Fc@Gr-Au, the charge reorganization is intensified over the Fc molecule, indicating more reactivity toward the cyclopentadienyl rings in the presence of the gold electrode. The Bader charges allow to investigate the charge transfer values on the model, indicating a quantitative representation. For the Gr-Au system, Bader charge analysis indicates that 0.022 electrons are donated from the graphene to the gold surface. The charge transferred from the Fc to the graphene monolayer is approximately 0.011 electrons for the Fc@Gr. For the entire system, (Fc@Gr-Au), the charges transferred from the Fc to the Au surface and graphene monolayer are approximately 0.044 and 0.016 electrons, respectively. On comparing cases Gr-Au and Fc@Gr-Au, it is noteworthy that the charge transfer to the Au electrode increases by a factor of 2, corroborating the experimental results that show an increase in the current density and hence, showed the enhanced electrochemical activity. The Gr-Au interaction can be understood as a key factor to promote the Fc charge transfer, since the system, Fc@Gr indicates a small transfer compared to the other systems.

The HET kinetics at the electrode surface involving the charge transfer between the electrode (graphene) and the redox molecules (Fc) can be modeled by applying the Mercus-Gerischer (MG) density of states (DOS) model to the redox system using the following equation[28,29]:

$$DOS^{red} = \frac{1}{\sqrt{4\lambda kT}} exp\left(-\frac{(E-eE^0-\lambda)^2}{4\lambda kT}\right) \qquad (1)$$

Where, DOS^{red} is related to redox molecule (Fc) reduced electronic state, λ is the reorganization energy, E^0 is the formal potential of redox couple ($Fc^{0/+1}$), e is the electronic charge, k is the Boltzmann constant, and T is the absolute temperature.

The possibility of the charge transfer is then determined by the simulation of the electronic DOS of graphene electrodes close to the Fermi level, as well as by identifying the number of oxidized electronic state of Fc for a reduction reaction, using eq. (1). These results are illustrated in Figure 4g: left panel shows the DFT DOS for Gr and Gr-Au systems; right panel presents the MG model distribution of the Fc electronic states. The previously observed enhanced HET kinetics between the graphene on the Au electrode and Fc (of the TCVD) can be explained based on the shift in the Fermi energy of graphene near its Dirac point. This shift in the energy level enables the overlapping between the graphene and Fc DOS; hence, facilitating

a faster electron transfer at the interface. The observed electrochemical shift of approximately 30 mV in the ΔE_p value of the Fc redox species; shown in Figure 4h, is reflected in the theoretical DOS results (Fig. 4g) indicating the increased reversibility of the interconversion of the redox species at the surface of the electrode. We also include the DFT results for the projected DOS (PDOS) for pristine graphene in a vacuum, Fc@Gr, Gr-Au, and Fc@Gr-Au (Fig. S9), as well as for the graphene and Gr-Au systems in the presence and absence of Fc under vacuum-aligned conditions (SI, S10). For pristine graphene, the Dirac cone shows at Fermi level (E=E_F), and the conduction is given by p_z electrons, as expected. For Fc@Gr (Fig. S9-b), the behavior is similar to the pristine one, i.e., the graphene Dirac cone appears at similar energies; however, there are two main peaks associated with ferrocene for negative energies close to E_F (-0.45 and -0.14 eV). Furthermore, three additional peaks were observed at both positive (+2.60 eV) and negative energies (-2.80 eV and -2.20 eV), also associated with Fc. For the Gr-Au system, the Au d-bands are noted approximately 1.00 eV below the Gr Dirac cone, and a slight displacement of the Dirac cone is observed by negative energies of approximately -0.08 eV, indicating graphene doping by the Au substrate. The Au DOS fills the entire energy range, showing the typical conduction type of the gold, and the Fc peaks remain unchanged (Fig. S9c-d). These results provide both qualitative and quantitative insights that allow us to infer that the role of the gold underneath is primarily related to facilitate electron transfer in the redox process of the top ferrocene layer by shifting the electronic states of the graphene.

TCVD device application in DNA biosensing. In this section we provide a proof-of-concept study of the biosensing properties of our TCVD device through EIS. For this, two different strategies were adopted; ds-DNA adsorption and DNA hybridization from the solution were detected using the device. The schematic of these two different experimental procedures is given in Figure 5a. From previous studies, it is well-known that any molecule adsorbed physically or attached chemically to the graphene surface can lead to an increase in the charge transfer resistance of the redox couple at the electrode/electrolyte interface[30,31]. The resultant changes can then be evaluated based on the increase in the diameter of the semicircle in the corresponding Nyquist plots. Contrary to this, we used a redox probe-free electrolyte, by monitoring the changes in the interfacial capacitance in the phosphate buffer solution (pH 7.2). The EIS spectra were recorded during the step-by-step fabrication of the device and its consequent sensing property measurements. From the Nyquist plots, the characteristic linear lines, indicating the absence of charge transfer, as well as the diffusive response for the pristine graphene on Au electrode (Figs. 5b, black curve) can be easily observed. Changes are observed in the linear profiles, either if Fc is adsorbed or ds-DNA is immobilized on the electrode surface. The process was monitored for a fixed concentration of ds-DNA (i.e 0.2 µmol L^{-1}). Similar results were obtained for the graphene without Au electrode (Fig. S11a).

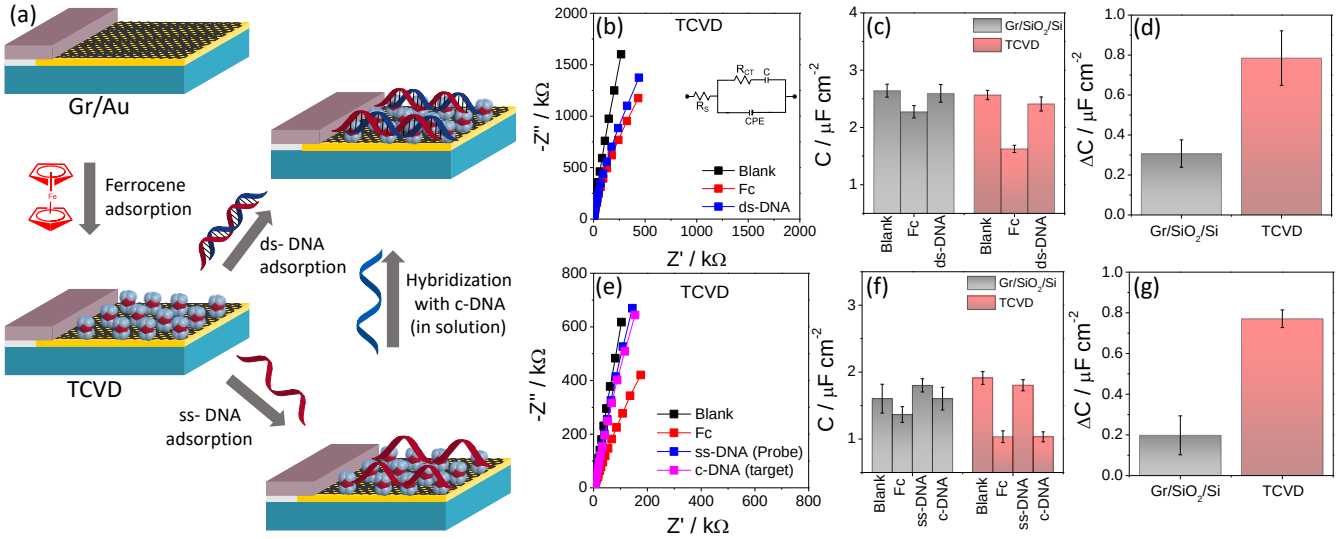

Figure 5: (a) Schematic illustration of ds-DNA adsorption and hybridization detection in solution of the TCVD; **(b)** Nyquist plots recorded in the phosphate buffer solution (0.1 mol.L^{-1}, pH 7.2) obtained during the adsorption of Fc and ds-DNA to the device surface; (**c**) plot of the measured capacitance of the TCVD and Gr/SiO_2/Si electrode obtained from fitting the Nyquist plots to the equivalent circuit (inset of Fig-b); (**d**) plot of the change in the capacitance after the adsorption of ds-DNA to the electrodes surface; (**e**) Nyquist plots of the TCVD electrode recorded in the phosphate buffer solution (0.1 mol.L^{-1}, pH 7.2) obtained during the adsorption of Fc, ss-DNA, and complementary DNA to the electrodes surface; (**f**) plot of the measured capacitance of the TCVD and Gr/SiO_2/Si electrode obtained from fitting the Nyquist plots to the equivalent circuit (inset of Fig-b); and (**g**) plot of change in the capacitance after the hybridization of the DNA on the electrode surface from the solution. The analyses were performed in triplicate (n = 3).

The semicircle is absent in the EIS spectra of the electrodes in the high frequency regime, due to the purely capacitive nature of the graphene electrodes (i.e., both pristine and immobilized with DNA). We followed the changes in the total interfacial capacitance from the simulation of equivalent circuit (inset of Fig. 5b) for each system. For this, the interfacial capacitance was modulated by a constant-phase element (CPE), whose impedance is described by equation (2). Z_{CPE} depends on A and p, this latter a frequency-independent parameter, which value ranges between $0 \leq p \leq 1$. Specifically, A is defined by equation (3), which is dependent on the relaxation time τ_0 and dielectric constant of the substrate ϵ_0, indicating that more conductive substrates should lead to smaller values of capacitance.[32]

The modeling of interfacial capacitance by CPE is frequently related to surface roughness and imperfections of the studied interfaces.[32] In our case, the interfacial capacitance concerns the individual capacitance contributions of an heterojunction consisted by Au, graphene, ferrocene, and DNA layers.

$$Z_{CPE} = A(i\omega)^{-p} \quad (2)$$

$$A = \frac{\tau_0^{(1-p)}}{(\epsilon_s - \epsilon_\infty)\epsilon_0} \quad (3)$$

Thus, the total capacitance can be considered as a result of a series association of the individual capacitance of each layer based on the interfacial capacitance evaluation of other graphene-electrolyte interfaces.[33] As frequently discussed in the literature[1,34,35], the contributions of graphene capacitance is given by its quantum capacitance (C_q), described by equation 4, and the recorded value is generally ~3 µF cm^{-2}. [35]

$$C_q = \frac{2e^2}{\pi} \cdot \frac{\sqrt{\pi n}}{\hbar \cdot v_F} \quad (4)$$

The values of capacitance obtained for the TCVD are shown in Figure 5c and compared with those of Gr/SiO_2/Si electrode. A greater surface sensitivity is observed for TCVD in terms of a higher decrease in the capacitance value when ferrocene is adsorbed on the electrode surface. Similarly, the observed change in capacitance is also very pronounced after the ds-DNA adsorption on the surface of electrode occurs. The values of capacitance obtained are 2.5 ± 0.08 and 2.6 ± 0.11 µF cm^{-2} for the TCVD and Gr/SiO_2/Si electrodes, respectively. The values change to 1.6 ± 0.06 and 2.3 ± 0.10 µF cm^{-2} in the presence of ferrocene and increase to 2.4 ± 0.10 and 2.6 ± 0.15 µF cm^{-2}, when ds-DNA is adsorbed on the electrodes surface. All the smaller values of total interfacial capacitance observed for TCVD system agree with the expected capacitance variation, according to the dependence of Z_{CPE} on the dielectric constant of the substrate. The changes in the values of the capacitance obtained for TCVD and Fc/Gr/SiO_2/Si electrode, after ds-DNA adsorption are 0.80 ± 0.10 µF cm^{-2} and 0.27 ± 0.08 µF cm^{-2}, respectively. This shows about three-fold higher surface sensitivity of the three-component device toward the ds-DNA adsorption to its surface (Fig. 5d). The TCVD was also tested for the detection of DNA hybridization in solution, containing nanomolar concentration (100 nmol L^{-1}) of the target single stranded DNA (complementary ss-DNA). In these experiments, the TCVD device previously modified with single stranded DNA (ss-DNA) probe was immersed in the solution and the EIS spectra were measured. Changes in the Nyquist plots were followed after each modification step (Fig. 5e) and the capacitance values were calculated. This procedure was repeated for the Fc/Gr/SiO_2/Si electrode (Fig. S11b). Initially, an increase in the capacitance value is noted

after the adsorption of ss-DNA on the electrode surface (Fig. 5f). The capacitance value then decreases, suggesting the hybridization between the two DNA strands. Since the ds-DNA is a rigid molecule and possibly detaches from the surface of electrode after hybridization[36], a decrease in the capacitance value is expected. From the comparison of the capacitance values obtained during the hybridization event on the surface of the electrodes, a larger variation in the values is observed for the TCVD system (Fig. 5g). The obtained capacitance value is approximately four times larger for the TCVD device than Fc/Gr system. These results show the consistent response for improved biomolecules detection of the three-component-based electrochemical device.

DISCUSSION

A combined experimental and theoretical investigation was conducted to describe the enhanced electrochemical activity and improved biosensing properties of the monolayer graphene-based electrode. The device, which we called TCVD, is composed of stacked van der Waals surfaces arranged vertically with the monolayer graphene sandwiched between the lithographically decorated subsurface Au on SiO_2/Si and top single layer ferrocene molecules. We demonstrate that TCVD devices exhibit remarkable electrochemical activities compared with conventional graphene-based vertical devices (graphene on SiO_2/Si surface).

It has been shown through covalent electron transfer chemistry that placing Au underneath graphene improves the poor chemical reactivity of the graphene by allowing the attachment of comparatively large number of organic functional groups to its surface. Au also enhances the sluggish electrochemical kinetics of a soluble redox probe at the graphene-electrolyte interface. This latter effect is attributed to the shift in the Fermi energy caused by the Au in graphene. We have shown experimentally that the ferrocene molecules have preferentially greater tendencies to adsorb to the graphene on Au surface. This is because of the change in the adsorptive properties of the graphene due to interaction between them. The enhanced electrochemical kinetics of the ferrocene on graphene on Au is then evidenced through the development of a theoretical model, showing the increased overlap between the density of state of graphene and ferrocene near the Fermi level due to the involvement of the underlying Au.

The underlying Au enhances the heterogeneous electron transfer (HET) kinetics and evidences a better electrochemical response. The enhanced electrochemical kinetics is firstly explained through the charge density difference, and then, by the combination of the charge transfer of the redox couple to the electrode with the Gerischer-Marcus model of HET kinetics. It is revealed that the newly developed system has a several times higher sensitivity in the adsorption and detection of biomolecules from the solution,

containing nanomole concentrations of the target molecule compared to the conventional graphene electrode, into which the designed electrode is immersed. Once ferrocene is adsorbed, the resultant three-component vdW surface now has a marked sensitivity to the attachment of the biological molecules, which was also revealed through the detection of DNA hybridization from the solution on the surface of the electrode. Based on the changes in the capacitance values obtained from the respective EIS spectrum for each modification step, it is claimed that this new system has a remarkable sensitivity for the detection of biomolecules and can be successfully implemented in the real-time biosensing applications.

CONCLUSION

The layer-by-layer stacking of a vdW surface involving monolayer graphene is an excellent way of enhancing the electrochemical activity of this 2D material because this procedure allows for the efficient exchange of charge transfer by increasing its charge carrier density. We have shown that the electron transfer kinetics of ferrocene on graphene on gold system is enhanced three times compared to that of conventional graphene on SiO_2/Si substrate. The improved kinetics of the designed system was also revealed through electrochemical measurements in the $[Fe(CN)_6]^{4-/3-}$ redox probe, in addition to the enhanced chemical reactivity demonstrated through electrochemical functionalization. Supporting DFT calculation were able to show, through DOS curves and the measurement of charge density, the difference of ferrocene on graphene on Au and without Au systems, that effective charge transfer occurs from the underlying Au due to the shift in the Fermi energy level of the graphene. Finally, the designed device was tested for the detection of ds-DNA adsorption and hybridization, showing a surface sensitivity five times higher than graphene on SiO_2/Si electrode in the presence of ferrocene; thus, opening the way for next-generation, vdW surface-based biosensors.

MATERIALS AND METHODS

Polymer mediated graphene transfer: The gold modified SiO_2/Si ($Au/SiO_2/Si$) substrate was initially prepared via a lithographic technique, in which a single Au/Ti micropattern (30 nm (20 nm Au and 10 nm Ti) in thickness and 0.04 cm^2 area) was obtained on the SiO_2/Si surface by placing a mask and then sputtered initially with Ti and then with gold by using a high-vacuum coating system (BAL-TEC, Liechtenstein). The graphene was then transferred to the prepared substrate as well as SiO_2/Si wafer (Graphene Supermarket) as described previously[37]. Briefly, about 10 µL of polystyrene (Sigma-Aldrich) solution (50 mg mL^{-1}) in toluene was initially drop-casted onto the surface of a small piece of Cu supported monolayer CVD grown graphene (Graphene Supermarket) and then dried at 70 °C in oven for 10 min. The Cu was

then removed through an etching solution (HCl and H_2O_2), leaving behind the graphene supported on polystyrene. From polystyrene the graphene was then transferred to SiO_2/Si and Au/SiO_2/Si substrates, and finally pre-annealed at 90 °C for 15 min. After cooling to room temperature, the polystyrene was then dissolved from the chip through toluene (Sigma Aldrich) and annealed at 585 °C for 1 min under inert (Ar) atmosphere. The obtained graphene electrodes were then etched electrochemically through cyclic voltammetry in the 0.1 mol L^{-1} HCl solution in the potential range from -1.0 to 1.0 V vs. Ag/$AgCl_{sat}$ at scan rate of 100 mV s^{-1} for 16 cycles, according to the previously published protocol[38], in order to remove the remaining Cu residue. The CVs of both electrodes obtained after various cycles are shown in Figure S12. In order to ensure that the electrolyte solution stays in contact only with graphene sheets, part of the electrodes was lithographically insulated with nitrocellulose resin at the boundary region between Pt/Ti film and graphene sheet. The Pt/Ti film was used as electrical contact to the graphene sheet.

Covalent functionalization: The covalent functionalization of the graphene electrodes was performed according to the previously published procedure[39]. Initially, a benzoic acid diazonium salt synthesized through a reaction between *p*-aminobenzoic acid (1×10^{-3} mol L^{-1}, Sigma-Aldrich) and sodium nitrite (5×10^{-3} mol L^{-1}, Sigma-Aldrich) in acidic medium (H_2SO_4, 1×10^{-2} mol L^{-1}) at 5 °C for 15 minutes. Using this reaction mixture as electrolyte, CV was performed in the potential range from -0.6 to +0.6 V at a scan rate of 50 mV s^{-1} (vs. Ag/$AgCl_{sat}$) for three cycles, which allows the electrochemical grafting of 4-carboxyphenyl functional groups to the surface of the graphene sheets. The electrodes were then rinsed several times with ultrapure water (18.2 MΩ cm) to remove any physically adsorbed species from their surfaces.

Electrochemical measurements: Electrochemical measurements of the graphene electrodes were performed using a three-electrode assembly connected to potentiostat/galvanostat (Autolab, PGSTAT128N) controlled by Nova software. Ag/$AgCl_{sat}$ reference electrode, Pt foil counter electrode, and monolayer graphene sheets supported on two different kinds of substrates were used as working electrodes. The electrochemical properties of the fabricated electrodes were evaluated by using two different redox probes: (i) Solution of $[Fe(CN)_6]^{4-}$/$[Fe(CN)_6]^{3-}$ (1×10^{-3} mol L^{-1}) in KCl (0.1 mol L^{-1}) was initially used to evaluate the electrochemical properties before and after covalent functionalization. Here, CV was performed in the potential range from -0.4 to +0.8 V at a scan rate of 100 mV s^{-1}. EIS of the electrodes was performed in the same electrolyte system as used for CV in the frequency range from 100 kHz to 0.1 Hz using a 5 mV sinusoidal potential and open circuit potential (OCP, 0.228 V) vs. Ag/$AgCl_{sat}$ as DC potential (ii) Ferrocene redox probe, for which 5 mg mL^{-1} of ferrocene in ethanol solution was directly drop-casted on the surface of the graphene surfaces. CV of the ferrocene-modified electrodes was then performed in KCl (0.1 mol L^{-}

^{1}) solution in the potential range from -0.2 to +0.6 V at different scan rates. All the potentials are quoted against $Ag/AgCl_{sat}$.

FTIR spectromicroscopy: FTIR spectra of the pristine and modified graphene electrodes were recorded in the micro ATR mode using 20× ATR lens with a Ge crystal at a spectral resolution of 4 cm^{-1} and 256 scans from 4000-600 cm^{-1} spectral window using FTIR spectrometer (Vertex 70v Bruker GmbH) coupled with FTIR microscope (Hyperion 3000, Bruker GmbH) and equipped with liquid N_2-cooled mercury cadmium telluride (MCT) detector.

Micro-Raman spectroscopy: Micro-Raman analysis was performed using micro-Raman spectrometer (Renishaw Model inVia) coupled with microscope (Leica) and equipped with charge couple device (CCD) detector. The excitation wavelength used was 514 nm. With the 50× objective lens of the Raman microscope, it is possible to collect spectra with 1 μm spatial resolution.

s-SNOM experiments: Scattering type scanning near field optical microscopy (s-SNOM) was performed using the IR1 beamline at the Brazilian Synchrotron Light Laboratory (LNLS). Initially, the collimated broadband IR radiation is passed through a Michelson interferometer (asymmetric), where its reference arm is blocked. The beam from the interferometer is then directed toward the tip of AFM cantilever probe, operating in the tapping mode with oscillating frequency ranges from 250 to 350 kHz. The backscattered light from the tip-sample interaction is then collimated and collected with the help of the lenses and finally combined with the reference beam and focused on the liquid N_2 cooled MCT detector of s-SNOM microscope. The detector response to the intensity of the scattered light are then recorded as phase sensitive images, showing the intensity of the second harmonic signal over the scanned area of the sample. The s-SNOM microscope is continuously purged with inert gas (N_2) to avoid possible interferences from atmospheric water vapor and CO_2.

Computational Details: The Au slab surface (111) was designed with 2×2×4 hexagonal layers, and graphene monolayer has similar structure. Both structures were adjusted in order to minimize the lattice parameter mismatch about 1%, following the procedures reported in the literature[40]. A vacuum of 18 Å was employed on the supercells. For the supercell was considered 48 gold atoms in 111 surface direction, 32 atoms for the graphene monolayer and 21 atoms for the Ferrocene molecule. The charge transfer mechanism was investigated using three different models: i) Ferrocene in a vacuum (Fc@vacuum) ii) Au and graphene monolayer (GR-Au); iii) Monolayer and Ferrocene (Fc@GR) and iv) Au, graphene monolayer and Ferrocene (Fc@GR-Au). These systems allow the influence analysis of each counterpart during the charge transfer process. The calculations were carried out within the Density Functional Theory (DFT) in the Kohn-Sham scheme[41], as implemented in the Quantum ESPRESSO[42,43]. The exchange correlation

functional employed is GGA-PBE[44] with van der Waals corrections as implemented by Klimes, Bowler and Michaelides[45]. It was employed Vanderbilt ultrasoft pseudopotentials, whereas the kinetic energy cutoff was chosen as 35 Ry, and 350 Ry for the description of the charge density. These parameters were carefully checked, assuring the interactions were well represented. In order to analyze the charge transfer results, it was evaluated the charge density difference of the system, and the quantitative values were investigated using the Bader charge model[46]. A vacuum of 18 Å was employed on the supercells. For the supercell was considered 48 gold atoms in 111 surface direction, 32 atoms for the graphene monolayer and 21 atoms for the Ferrocene molecule. The charge transfer mechanism was investigated using three different models: i) Au and graphene monolayer (GR-Au); ii) Monolayer graphene and Ferrocene (Fc@GR) and iii) Au, graphene monolayer and Ferrocene (Fc@GR-Au). These systems allow the influence analysis of each counterpart during the charge transfer process.

Adsorption of ds-DNA and hybridization detection: Double-stranded DNA (ds-DNA) was prepared by mixing 20^{A} (5′-GTG AGC TAA CGT GTC AGT AC-3′) and 20^{T} (5′-GTA CTG ACA CGT TAG CTC AC-3′) at 1:1 mole ratio with a final concentration of 4 μmol L^{-1} and annealing them by heating to 90 □C followed by slowly cooling them to room temperature. For the adsorption of the ds-DNA, approximately 5 μL in phosphate buffer (pH 7.2) was directly drop-casted on the surface of electrodes, allowed for about 5 minutes on the surface of electrode, washed several times with de-ionized water, then performing the electrochemical impedance spectroscopy in the phosphate buffer in the frequency range of 1 MHz to 100 mHz with an ac amplitude of 5 mV and at open cell potential (OCP). For the DNA hybridization detection in solution, ss-DNA probe (2 μmol L^{-1}) was initially immobilized on the surface of electrodes for about 30 minutes, washed several times with de-ionized water and then immersed in a phosphate buffer (pH 7.2) containing 100 nmol L^{-1} of the complementary ss-DNA (target), followed by the measurements of the electrochemical impedance spectroscopy.

AUTHOR INFORMATION

Corresponding Author

* frankcrespilho@iqsc.usp.br

Author Contributions

These authors contributed equally to this manuscript.

Notes

The authors declare no competing financial interest.

ACKNOWLEDGMENT

The authors greatly appreciate the financial support of the São Paulo Research Foundation (FAPESP) (Projects: 2019/15333-1, 2019/12053-8, 2017/20493-2 and 2018/11071-0) and the National Council for Scientific and Technological Development (CNPq) (Project: 428211/2018-6). A.H. thanks the Coordinating Agency for Advanced Training of Graduate Personnel (CAPES-PNPD) (Process: 88887.358060/2019-00) for the postdoctoral fellowship. R.G.A. also acknowledges the financial support from the FAPERJ under grant numbers (E-26/010.101126/201 and E-26/202.699/2019), and CNPq (2535/2017-1 and 437182/2018-5). The computational time was provided by CENAPAD/SP and SICC-PRP/IFSP. The authors thank LNLS for providing the beamtime as well as Dr. Raul O. Freitas and Mr. Thiago M. D. Santos for their technical support.

REFERENCES

1 W. Fu, L. Feng, D. Mayer, G. Panaitov, D. Kireev, A. Offenhäusser and H. J. Krause, *Nano Lett.*, 2016, **16**, 2295–2300.

2 B. Zhan, C. Li, J. Yang, G. Jenkins, W. Huang and X. Dong, *Small*, 2014, **10**, 4042–44065.

3 T. Deng, Z. Zhang, Y. Liu, Y. Wang, F. Su, S. Li, Y. Zhang, H. Li, H. Chen, Z. Zhao, Y. Li and Z. Liu, *Nano Lett.*, 2019, **19**, 1494–1503.

4 Z. Wang, K. Yi, Q. Lin, L. Yang, X. Chen, H. Chen, Y. Liu and D. Wei, *Nat. Commun.*, 2019, **10**, 1–9.

5 P. Ahlberg, M. Hinnemo, M. Song, X. Gao, J. Olsson, S. L. Zhang and Z. B. Zhang, *Appl. Phys. Lett.*, 2015, **107**, 203104–1.

6 Y. R. Kim, T. L. Phan, Y. S. Shin, W. T. Kang, U. Y. Won, I. Lee, J. E. Kim, K. Kim, Y. H. Lee and W. J. Yu, *ACS Appl. Mater. Interfaces*, 2020, **12**, 10772–10780.

7 X. Chen, T. Wu and W. Zhuang, *Nanoscale*, 2020, 8793–8800.

8 Y. Liu, Z. Gao, Y. Tan and F. Chen, *ACS Nano*, 2018, **12**, 10529–10536.

9 A. K. Geim and I. V. Grigorieva, *Nature*, 2013, **499**, 419–425.

10 L. Britnell, R. V. Gorbachev, R. Jalil, B. D. Belle, F. Schedin, A. Mishchenko, T. Georgiou, M. I. Katsnelson, L. Eaves, S. V. Morozov, N. M. R. Peres, J. Leist, A. K. Geim, K. S. Novoselov and L. A. Ponomarenko, *Science (80-.).*, 2012, **335**, 947–950.

11 H. Yang, J. Heo, S. Park, H. J. Song, D. H. Seo, K. E. Byun, P. Kim, I. K. Yoo, H. J. Chung and K. Kim, *Science (80-.).*, 2012, **336**, 1140–1143.

12 A. Avsar, T. Y. Yang, S. Bae, J. Balakrishnan, F. Volmer, M. Jaiswal, Z. Yi, S. R. Ali, G. Guöntherodt, B. H. Hong, B. Beschoten and B. Özyilmaz, *Nano Lett.*, 2011, **11**, 2363–2368.

13 G. Giovannetti, P. A. Khomyakov, G. Brocks, V. M. Karpan, J. Van Den Brink and P. J. Kelly, *Phys. Rev. Lett.*, 2008, **101**, 4–7.

14 G. L. C. Paulus, Q. H. Wang and M. S. Strano, *Acc. Chem. Res.*, 2013, **46**, 160–170.

15 J. Rafiee, X. Mi, H. Gullapalli, A. V. Thomas, F. Yavari, Y. Shi, P. M. Ajayan and N. A. Koratkar, *Nat. Mater.*, 2012, **11**, 217–222.

16 Y. Y. Wang, Z. H. Ni, T. Yu, Z. X. Shen, H. M. Wang, Y. H. Wu, W. Chen and A. T. S. Wee, *J. Phys. Chem. C*, 2008, **112**, 10637–10640.

17 S. Nie, N. C. Bartelt, J. M. Wofford, O. D. Dubon, K. F. Mccarty and K. Th, *Phys. Rev. B*, 2012, **85**, 205406.

18 Z. Ao, M. Jiang, Z. Wen and S. Li, *Nano Res. Lett.*, 2012, **7**, 1–6.

19 L. J. A. Macedo, F. C. D. A. Lima, R. G. Amorim, R. O. Freitas, A. Yadav, R. M. Iost, K. Balasubramanian and F. N. Crespilho, *Nanoscale*, 2018, **10**, 15048–15057.

20 R. L. Mccreery, *Chem. Rev.*, 2008, **108**, 2646–2687.

21 D. A. C. Brownson and C. E. Banks, *Phys. Chem. Chem. Phys.*, 2011, **13**, 15825–15828.

22 D. A. C. Brownson and C. E. Banks, *Phys. Chem. Chem. Phys.*, 2012, **14**, 8264–8281.

23 M. Marandi, K. Tammeveski, M. Lillethorup, M. Kongsfelt, S. U. Pedersen, B. B. E. Jensen, K. Daasbjerg, A. B. Mortensen, V. Sammelselg and E. Kibena, *Electroanalysis*, 2014, **26**, 2619–2630.

24 H. Liu, Y. Liu and D. Zhu, *J. Mater. Chem.*, 2011, **21**, 3335–3345.

25 I. Heller, J. Kong, K. A. Williams, C. Dekker and S. G. Lemay, *J. Am. Chem. Soc.*, 2006, **128**, 7353–7359.

26 P. A. Khomyakov, G. Giovannetti, P. C. Rusu, G. Brocks, J. Van Den Brink and P. J. Kelly, *Phys. Rev. B - Condens. Matter Mater. Phys.*, 2009, **79**, 1–12.

27 B. Tincu, I. Demetrescu, A. Avram, V. Tucureanu, A. Matei, O. Tutunaru, T. Burinaru, F. Comanescu, C. Voitincu and M. Avram, *Diam. Relat. Mater.*, 2019, **98**, 107510.

28 M. Rudolph and E. L. Ratcliff, *Nat. Commun.*, 2017, **8**, 1–6.

29 J. H. Zhong, J. Zhang, X. Jin, J. Y. Liu, Q. Li, M. H. Li, W. Cai, D. Y. Wu, D. Zhan and B. Ren, *J. Am. Chem. Soc.*, 2014, **136**, 16609–16617.

30 S. Eissa, G. C. Jimenez, F. Mahvash, A. Guermoune and C. Tlili, *Nano Res.*, 2015, **8**, 1698–1709.

31 N. Zainudin, A. R. Mohd Hairul, M. M. Yusoff, L. L. Tan and K. F. Chong, *Anal. Methods*, 2014, **6**, 7935–7941.

32 E. Barsoukov and J. R. Macdonald, *Impedance Spectroscopy: Theory, Experiment, and Applications*, John Wiley & Sons, Hoboken, New Jersey, 2005.

33 Y. Ohno, K. Maehashi, Y. Yamashiro and K. Matsumoto, *Nano Lett.*, 2009, **9**, 3318–3322.

34 J. Liu, Q. Li, Y. Zou, Q. Qian, Y. Jin, G. Li, K. Jiang and S. Fan, *Nano Lett.*, 2013, **13**, 6170–6175.

35 N. C. S. Vieira, J. Borme, G. Machado, F. Cerqueira, P. P. Freitas, V. Zucolotto, N. M. R. Peres and P. Alpuim, *J. Phys. Condens. Matter*, 2016, **28**, 1–9.

36 O. Zagorodko, J. Spadavecchia, A. Y. Serrano, I. Larroulet, A. Pesquera, A. Zurutuza, R. Boukherroub and S. Szunerits, *Anal. Chem.*, 2014, **86**, 11211–11216.

37 N. L. Ritzert, W. Li, C. Tan, G. G. Rodr, J. J. Parks and D. C. Ralph, *Faraday Discuss.*, 2014, **172**, 27–45.

38 R. M. Iost, F. N. Crespilho, L. Zuccaro, H. K. Yu, A. M. Wodtke, K. Kern and K. Balasubramanian, *ChemElectroChem*, 2014, **1**, 2070–2074.

39 S. Sarkar, E. Bekyarova and R. C. Haddon, *Mater.Today*, 2012, **15**, 276–285.

40 M. Benoit, C. Langlois, N. Combe, H. Tang and M.-J. Casanove, *Phys. Rev. B*, 2012, **86**, 075460.

41 W. Kohn and L. J. L. J. J. Sham, *Phys. Rev.*, 1965, **140**, A1133–A1138.

42 P. Giannozzi, S. Baroni, N. Bonini, M. Calandra, R. Car, C. Cavazzoni, D. Ceresoli, G. L. Chiarotti, M. Cococcioni, I. Dabo, A. Dal Corso, S. De Gironcoli, S. Fabris, G. Fratesi, R. Gebauer, U. Gerstmann, C. Gougoussis, A. Kokalj, M. Lazzeri, L. Martin-Samos, N. Marzari, F. Mauri, R. Mazzarello, S. Paolini, A. Pasquarello, L. Paulatto, C. Sbraccia, S. Scandolo, G. Sclauzero, A. P. Seitsonen, A. Smogunov, P. Umari and R. M. Wentzcovitch, *J. Phys. Cond. Matter*, 2009, **21**, 395502 (19pp).

43 J. Enkovaara, C. Rostgaard and J. J. Mortensen, *J. Phys. Condens. Matter*, 2017, **29**, 465901.

44 J. P. Perdew, K. Burke and M. Ernzerhof, *Phys. Rev. Lett.*, 1996, **77**, 3865–3868.

45 J. Klimeš, D. R. Bowler and A. Michaelides, *J. Phys. Condens. Matter*, 2010, **22**, 022201.

46 G. Henkelman, A. Arnaldsson and H. Jónsson, *Comput. Mater. Sci.*, 2006, **36**, 354–360.

Supporting information

A three component-based van der Waals surface vertically designed for biomolecular recognition enhancement

Ayaz Hassan[†], Lucyano J. A. Macedo[†], Isabela A. Mattioli[†], Rafael J. G. Rubira[#], Carlos J. L. Constantino[#], Rodrigo G. Amorim[§], Filipe C. D. A. Lima[‡], Frank N. Crespilho[†]*

[†]São Carlos Institute of Chemistry, University of São Paulo, 13560-970 São Paulo, Brazil
[§]Physics Departament, ICEx, Fluminense Federal University – UFF, Volta Redonda, 27213-145, Rio de Janeiro, Brazil
[‡]Federal Institute of Education, Science, and Technology of São Paulo, Campus Matão, 15991-502 São Paulo, Brazil
[#]Physics Department, São Paulo State University-UNESP, Campus of Presidente Prudente, SP 19060-900, Brazil

Figure S1

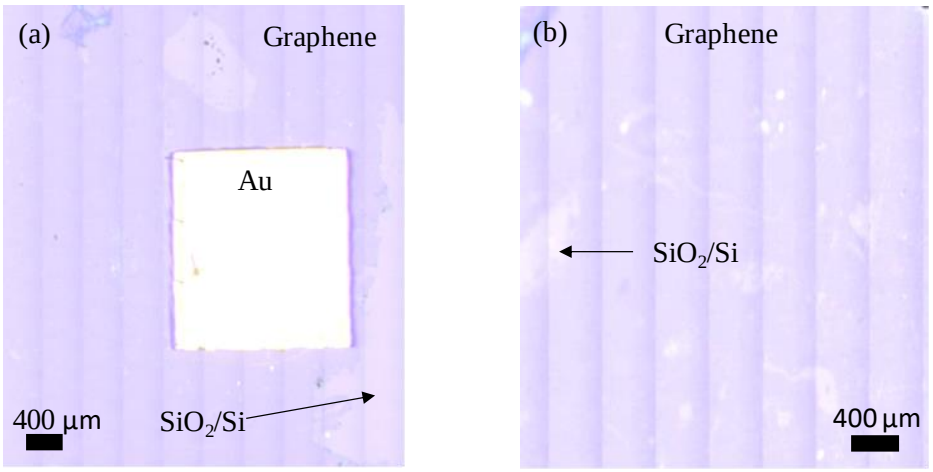

Figure S1 – Optical microscopic images of (**a**) Gr/Au/SiO_2/Si and (**b**) Gr/SiO_2/Si electrodes.

S2: Covalent functionalization of graphene electrodes.

The electrodes were characterized for their chemical reactivities through a standard covalent functionalization procedure[1], commonly used for modifying the carbon electrodes, which involves the attachment of the in situ generated aryl radicals from the solution onto the surface of the electrode, when an external electrochemical potential is applied. For this purpose, cyclic voltammetry was performed in the reaction mixture containing 4-amino benzoic acid, $NaNO_2$ and H_2SO_4 in the potential range of +0.6 to -0.6 at a scan rate of 50 mV s^{-1} during two cycles. An irreversible reduction wave observed during the first cycle of voltammetric scan (Figure 1b-c, main manuscript and Figure S2b) is consistent with the one electron reduction of the diazonium cations and their subsequent anchoring to the electrode surface. The reduction wave cannot be observed at this position in the subsequent second scan, indicating the complete saturation of the electrode surface with organic functional groups during the first voltammetric scan. The surface concentrations of the organic functional groups attached during the covalent functionalization were calculated for all the electrodes by using the following equation[2]:

$$\Gamma = \frac{Q}{n.F.A} \qquad \text{S1}$$

where Q is the faradaic charge obtained by the integration of the reduction wave in the CV after subtracting the contribution of capacitive current, n is the number of electrons involved (here n = 1), F is the Faraday constant and A is the geometric area of the electrode.

Table S1: Reduction peak potential, onset potential and surface concentration of the electrochemically reduced 4-carboxyphenyl organic moieties on the surface obtained from the cyclic voltammograms of Gr/Au/SiO_2/Si, Gr/SiO_2/Si, and Au thin film electrodes.

Electrode	**Reduction peak potential (mV)**	**Onset potential (mV)**	**Surface coverage (Γ, mol cm^{-2})**
Gr/Au/SiO_2/Si	-221	250 mV	4.3×10^{-9}
Gr/SiO_2/Si	-285	50 mV	2.3×10^{-10}
Au film electrode (no graphene)	-77 and 63	300 mV	4.3×10^{-8}

Figure S2

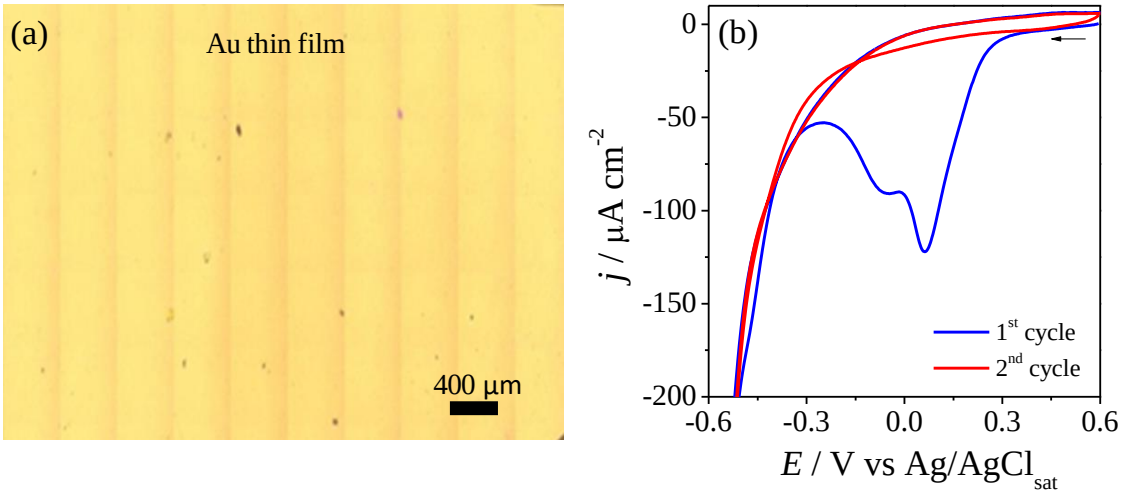

Figure S2 – (a) Optical microscopic image of flat Au film electrode (b) Cyclic voltammograms obtained during the covalent functionalization of the flat Au film electrode performed electrochemically in the reaction mixture containing 4-amino benzoic acid, $NaNO_2$ and H_2SO_4 in the potential range of +0.6 to -0.6 at a scan rate of 50 mV s^{-1} during three cycles.

S3: Quantification of defects density using micro-Raman spectroscopy

For the estimation of defects density after the D-band appeared in the Raman spectra of the covalently functionalized electrodes, the ratio of the intensity of the D peak to G peak (I_D/I_G) is used. Once the I_D/I_G values are obtained (Table S2), the defects density are calculated for each electrode using the following empirical equation[3,4]:

$$\frac{I_D}{I_G} = C_A \cdot \frac{r_a^2 - r_s^2}{r_a^2 - 2r_s^2}\left[\exp\left(\frac{-\pi \cdot r_s^2}{L_D^2}\right) - \exp\left(\frac{-\pi\left(r_a^2 - r_s^2\right)}{L_D^2}\right)\right] + C_S \cdot \left[1 - \exp\left(\frac{-\pi \cdot r_s^2}{L_D^2}\right)\right] \qquad \text{S2}$$

Where L_D is the distance between the defects, r_s and r_a are the parameters related to the radii of the structurally damaged and activated region around each defective site, respectively. Based on the excitation laser wavelength, 514 nm, used in this study the values of parameters used in the above equation are C_A = 5, Cs = 0.86, r_a = 1.8 nm, and r_s = 1 nm, which results in the plot shown in Figure S3. The plot shown correlates the I_D/I_G to the distance of the defects (L_D) and is usually used to illustrate the quality of the graphene electrodes[3,4]. Based on the L_D values obtained from the corresponding plot, the defect density values are calculated by using the following the equation.

$$n_D = \frac{10^{14}}{\pi L_D^2} \qquad \text{S3}$$

Figure S3

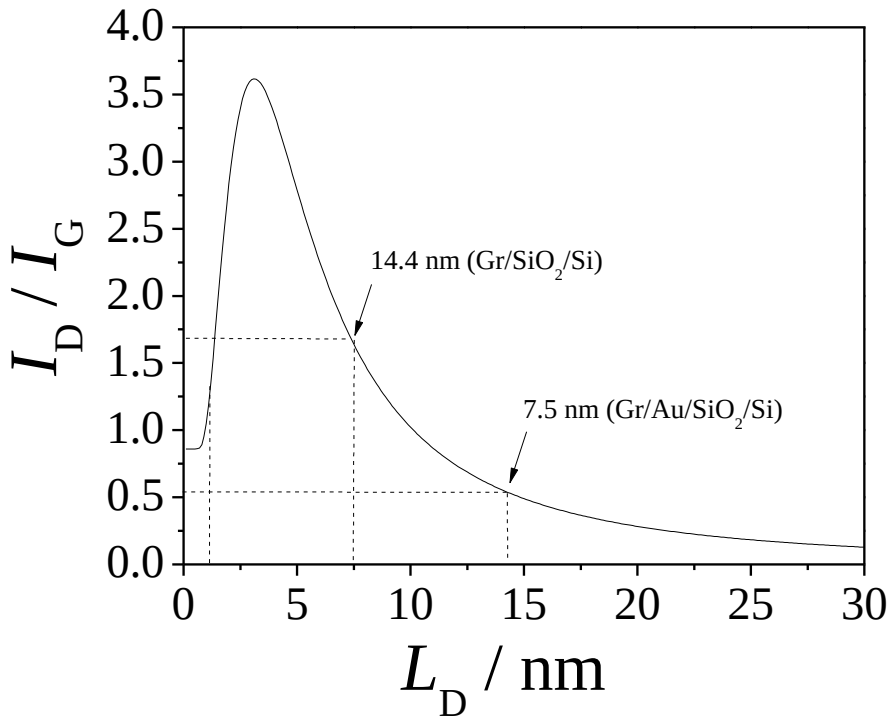

Figure S3 – Fitted I_D/I_G ratio as a function of the mean distance between defects (L_D) for the Gr/Au/SiO_2/Si and Gr/SiO_2/Si electrodes.

Table S2: Values of parameters obtained from the Raman spectra of the pristine and functionalized electrodes with and without gold subsurface.

Electrode	**Peak position (G-band, cm^{-1})**	**Peak position (2D band, cm^{-1})**	**Peak Intensity G-band)**	**Peak Intensity (D band)**	**FWHM (2D-band, cm^{-1})**	I_D/I_G
Gr/Au/SiO_2/Si pristine	1582	2685	353	---	29	
Gr/Au/SiO_2/Si functionalized	1588	2700	877	467	43	0.53
Gr/SiO_2/Si pristine	1587	2693	4075	---	35	
Gr/SiO_2/Si functionalized	1589	2690	4070	6725	37	1.65

Figure S4

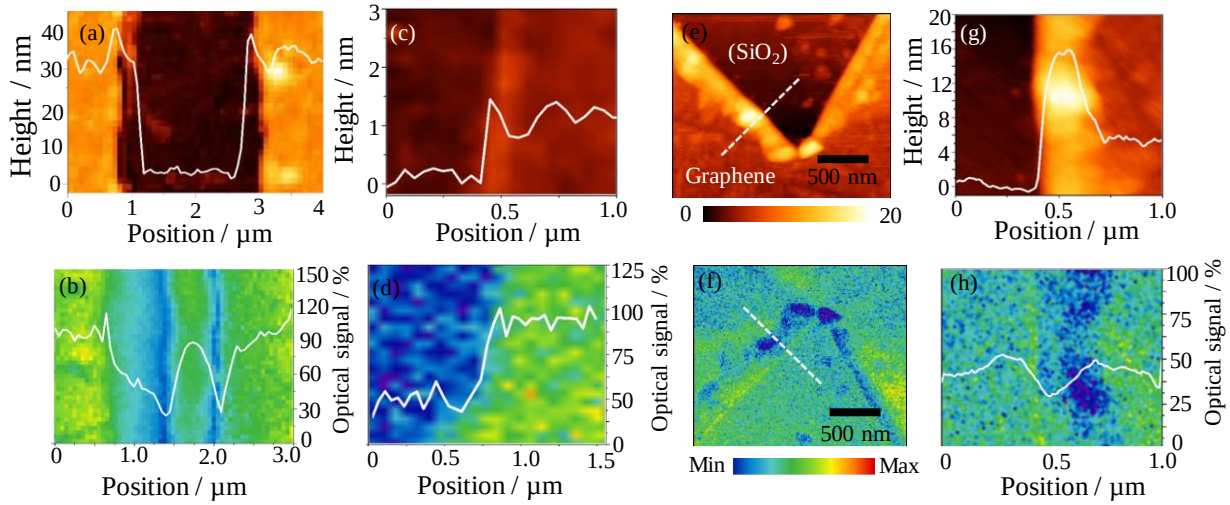

Figure S4 - (**a**) Height profile of the graphene in the boundary region between SiO_2/Si and Au (**b**) IR broadband image of the boundary region between SiO_2/Si and Au; (**c**) height profile in the boundary region between SiO_2/Si and graphene (**d**) IR broadband signal profile in the boundary region between graphene and SiO_2/Si; (**e**) topography and (**f**) IR broadband image in the boundary region between graphene and SiO_2/Si of the functionalized graphene on SiO_2/Si substrate, (**g**) height profile and (**h**) IR broadband signal profile in the boundary region between graphene and SiO_2/Si substrate.

Figure S5

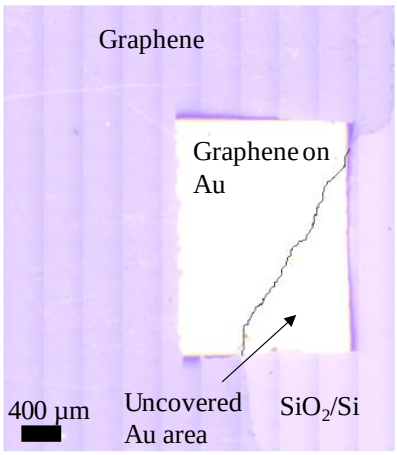

Figure S5 – Optical microscopic image of the Gr/Au/SiO_2/Si electrode with uncovered Au subsurface area. The line between the covered and uncovered Au area by the graphene sheet is drawn roughly.

Figure S6

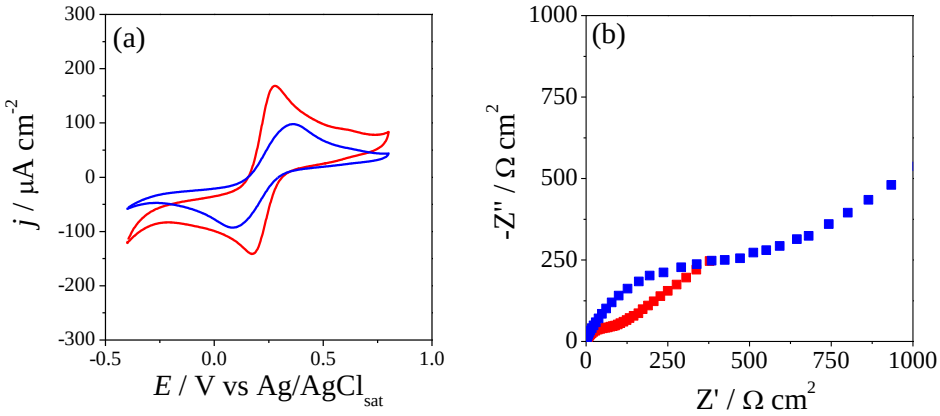

Figure S6 – (**a**) Cyclic voltammograms and (**b**) EIS spectra of the electrodes recorded in $[Fe(CN)_6]^{4-/3-}$ (1×10^{-3} mol L^{-1}) and KCl (0.1 mol L^{-1}). (—) Gr/Au/SiO_2/Si electrode with exposed Au area and (—) Au thin film electrode. Scan rate in (a): 50 mV s^{-1}.

Figure S7

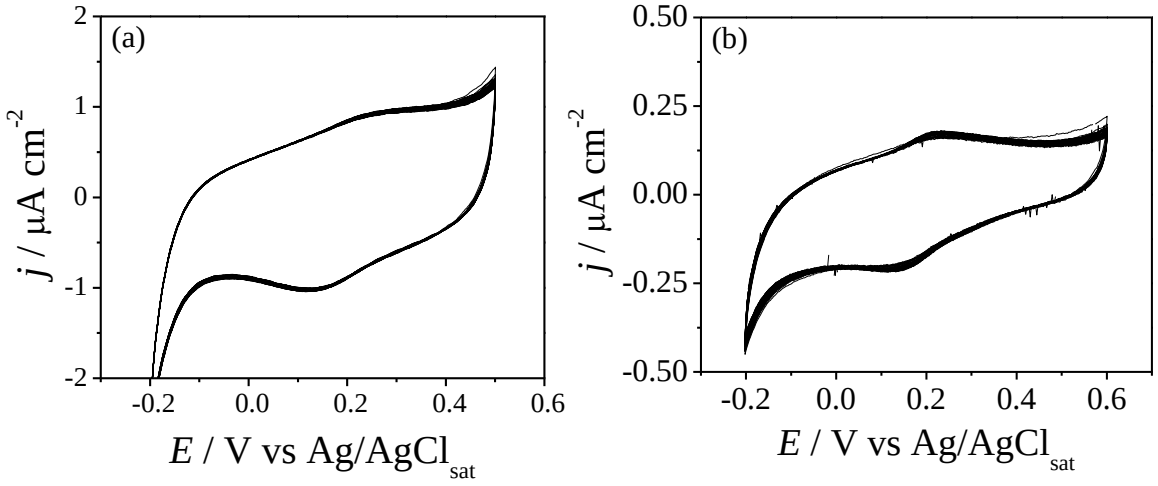

Figure S7 – Cyclic voltammograms of the ferrocene dissolution from the surface of (**a**) Gr/Au/SiO_2/Si and (**b**) Gr/SiO_2/Si electrodes obtained in the KCl (0.1 mol L^{-1}) at a scan rate of 50 mV s^{-1}.

S8: Determination of heterogeneous electron transfer (HET) rate constant (k^0).

From the steady state CV response, the anodic peak current (j_{pa}) and cathodic peak current (j_{pc}) densities values after the proper subtraction of background current were plotted against the increasing scan rate (ν) (Figure S8 insets). As expected, a linear relationship of both the j_{pa} and j_{pc} as function of ν was obtained for both electrodes, which indicates the redox process to be confined to the surfaces of the electrodes. The heterogeneous electron transfer (HET) rate constants are determined for both electrodes, using the mathematical approach proposed by Laviron (based on Butler-Volmer theory)[5], where the values of anodic and cathodic peaks overpotential; (E_{pa}-E^0) and (E_{pc}-E^0) calculated from the CVs are plotted as a function of log (v) (inset of Fig. S8). From the slopes of the linear regions of the plot, the values of transfer co-efficient (α) are determined and then electron transfer rate constants (k^0) are calculated by using the equation S4:

$$k^0 = \frac{\alpha n F \nu_c}{RT} = \frac{(1-\alpha) n F \nu_a}{RT} \qquad \text{S4}$$

Figure S8

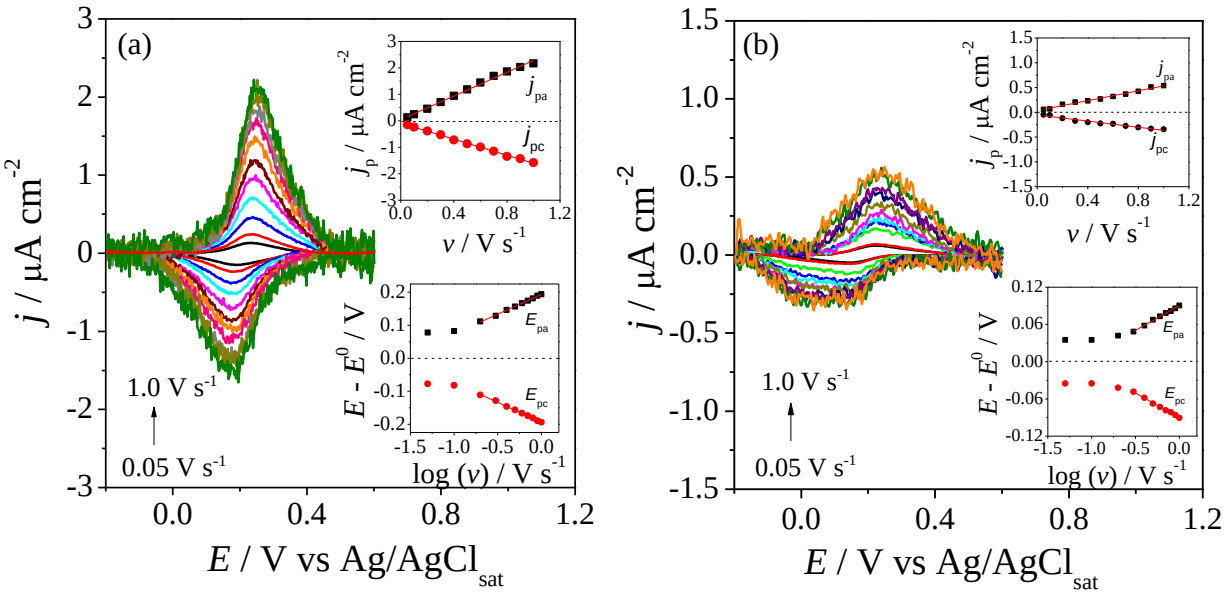

Figure S8 – Anodic and cathodic peak current densities at different scan rates of (**a**) Gr/Au/SiO_2/Si and (**b**) Gr/SiO_2/Si electrodes. The insets in (a) and (b) are the plots of anodic and cathodic peak current densities as a function of scan rate (top right) and Laviron plots (bottom right).

Figure S9

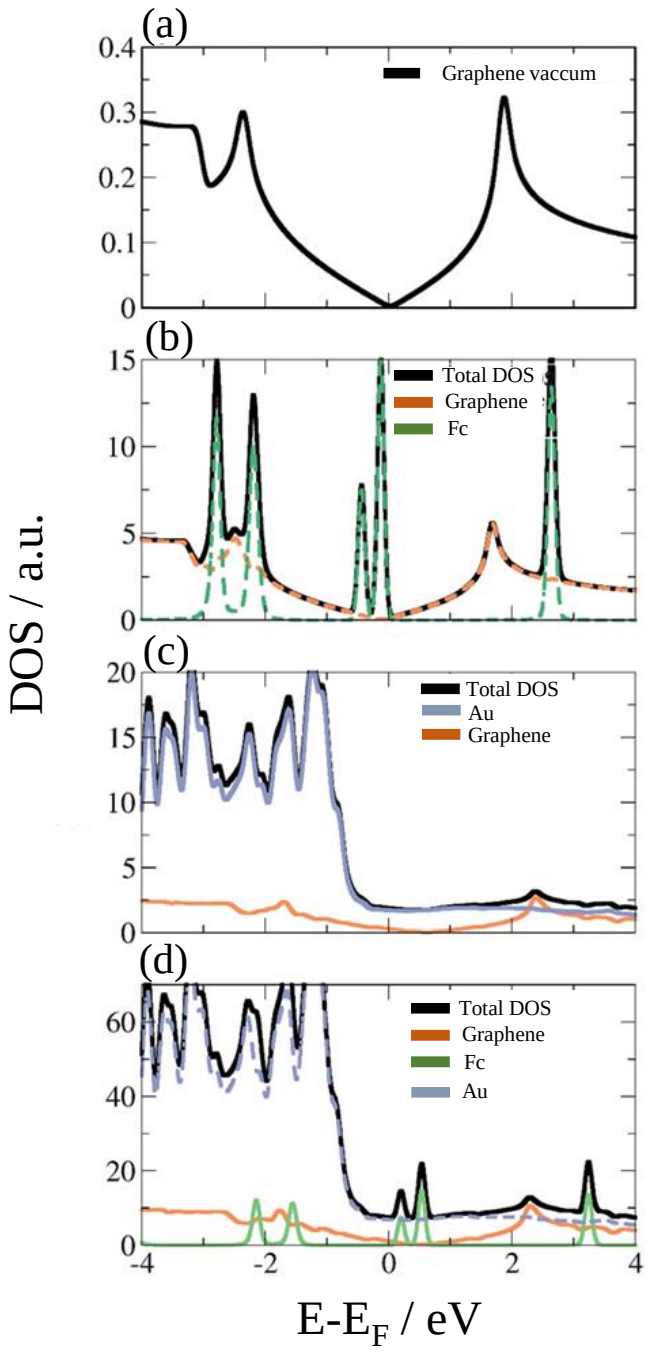

Figure S9 – Projected DOS for the (**a**) Isolated Graphene, (**b**) Fc@Gr, (**c**) Gr-Au, and (**d**) Fc@Gr-Au systems.

S10: Projection of Gr electronic states for pristine graphene, Fc@Gr, Au@Gr, and Fc@Gr-Au with the alignment of the pristine Gr vacuum level using DFT simulations.

Projected DOS for the graphene and graphene on Au in the absence and presence of ferrocene. These DOS were obtained by aligning the vacuum level of the pristine graphene, as shown in the computational details. As shown in Figure S10, it can be observed that Fc shifts Gr's electronic structure to negative energies, about -0.06 eV. On the other hand, the Au surface presence shifts +0.6 eV for Gr only, and +0.58 eV in the entire system (Fc@Gr-Au) and it interacts with graphene as shown by the orange and for the whole system blue curves.

Figure S10

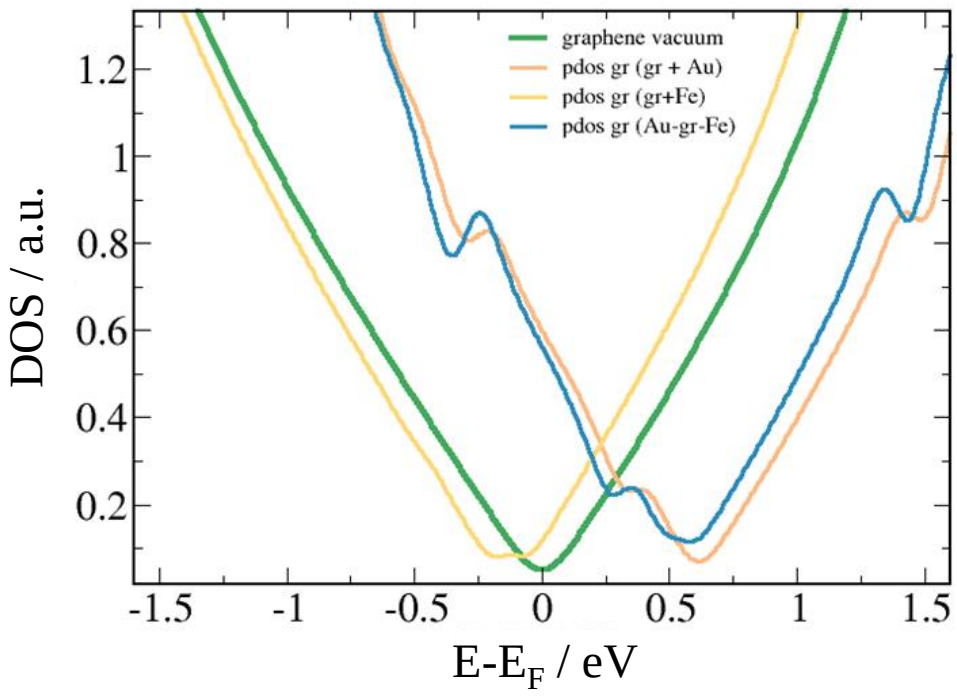

Figure S10 – Projected density of state (PDOS) under vacuum aligned conditions for the (—) isolated graphene, (—) Fc@Gr, (—) Gr-Au, and (—) Fc@Gr-Au systems.

Figure S11

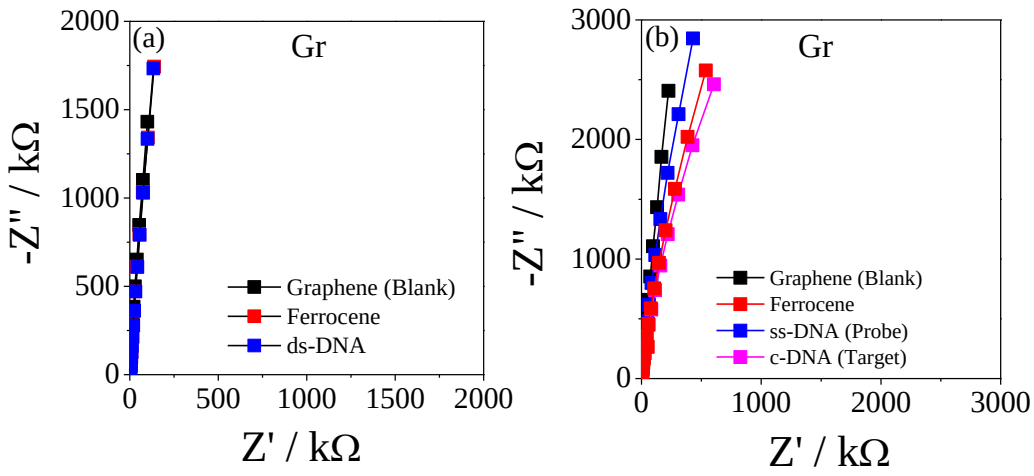

Figure S11 – (**a**) Nyquist plots recorded during the adsorption of Fc and ds-DNA on the surface of $Gr/SiO_2/Si$ electrode in the phosphate buffer solution (0.1 mol L^{-1}, pH 7.2) in the frequency range of 1 MHz to 100 mHz with an ac amplitude of 5 mV and at open cell potential (OCP) and (**b**) Nyquist plots obtained during the detection of hybridization of the complementary DNA in solution on the surface of $Gr/SiO_2/Si$ electrode previously modified with single strand DNA (ss-DNA) probe in the presence of ferrocene.

Figure S12

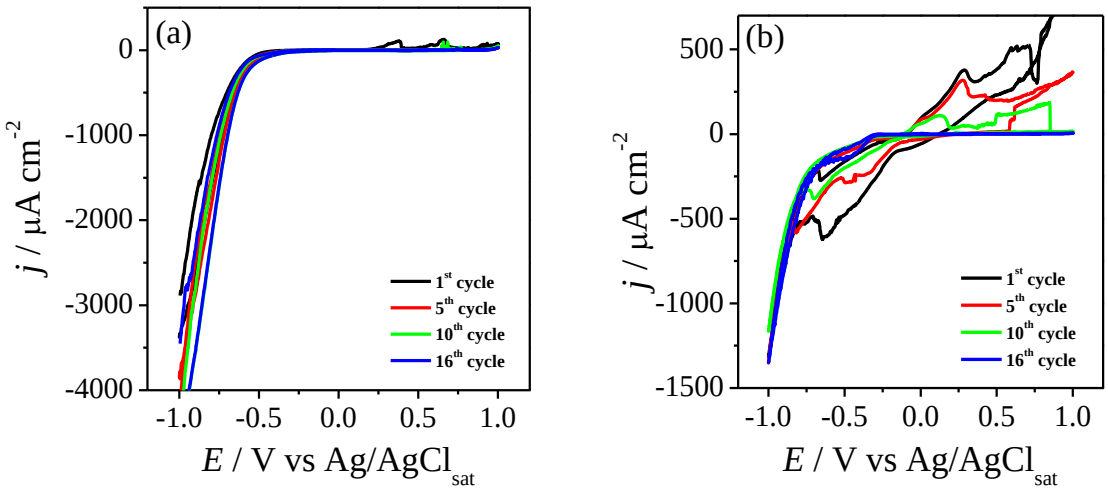

Figure S12 – Cyclic voltammograms obtained after various cycles during the electrochemical etching process performed in HCl (0.1 mol L^{-1}) in the potential range of -1.0 to +1.0 V for 16 cycles. (**a**) Gr/Au/SiO_2/Si and (**b**) Gr/SiO_2/Si electrodes. Scan rate: 100 mV s^{-1}.

References

1 M. Kullapere, J.-M. Seinberg, U. Mäeorg, G. Maia, D. J. Schiffrin and K. Tammeveski, *Electrochim. Acta*, 2009, **54**, 1961–1969.

2 L. J. A. Macedo, F. C. D. A. Lima, R. G. Amorim, R. O. Freitas, A. Yadav, R. M. Iost, K. Balasubramanian and F. N. Crespilho, *Nanoscale*, 2018.

3 M. M. Lucchese, F. Stavale, E. H. M. Ferreira, C. Vilani, M. V. O. Moutinho, R. B. Capaz, C. A. Achete and A. Jorio, *Carbon N. Y.*, 2010, **48**, 1592–1597.

4 L. G. Cançado, A. Jorio, E. H. M. Ferreira, F. Stavale, C. A. Achete, R. B. Capaz, M. V. O. Moutinho, A. Lombardo, T. S. Kulmala and A. C. Ferrari, *Nano Lett.*, 2011, **11**, 3190–3196.

5 R. A. S. Luz and F. N. Crespilho, *RSC Adv.*, 2016, **6**, 62585–62593.